Influence of Structural Properties on Fusion Cross-Sections Using Proximity Potentials

Lina S. Abdalmajid and Adil M. Saeed†

Department of Physics, College of Science, University of Sulaimani, Sulaymaniyah, Kurdistan Region, F.R. Iraq

Abstract—**In this study, an optimal nuclear proximity potential is used to get more accurate fusion cross-section predictions. For 111 colliding systems, we evaluate the predictive accuracy of several proximity potential models interfaced with Wong's formula in reproducing the fusion cross-section experimental data. For the purpose of Chi-square minimization technique, Christensen and Winther 1976 potential is selected. The analysis examines fusion dynamics across a wide range of nuclear configurations ($6 \leq Z_p$ (projectile atomic number)≤ 28, $6 \leq Z_t$ (target atomic number) ≤ 94, and $36 \leq Z_p Z_t \leq 1880$). To increase accuracy and match experimental data, a Python code that calculates cross-sections for all proximity potentials is established using the Nelder–Mead algorithm. The extensive range of calculations facilitates a systematic study of the effects of structural factors, including magic numbers, shell structure, neutron excess, and pairing effect. The results reveal that shell effects can sometimes overcome neutron excess and produce unexpected fusion trends, as seen in the ^{28}Si + ^{90}Zr and ^{28}Si + ^{94}Zr. In other reactions, the shell effect eliminated the effect of the neutron excess, such as in the ^{16}O + ^{62}Ni versus ^{16}O + ^{58}Ni and ^{12}C + ^{208}Pb versus ^{12}C + ^{204}Pb reactions. Our findings also highlighted the important role of the projectile in the process of fusion. The titanium isotopes (^{46}Ti, ^{50}Ti) in particular fused more effectively with ^{12}C than with ^{16}O. Nickel isotopes show similar projectile-dependent behavior.**

***Index Terms*—Fusion cross-sections, Magic numbers effect, Mean difference, Neutron excess effect, Proximity potentials, Shell structure effect.**

I. Introduction

Recent decades have witnessed extensive theoretical and experimental investigation into heavy-ion fusion (HIF) (Zhang, Liu and Lin, 2014). Calculating theoretical HIF cross-sections requires a well-understood nucleus-nucleus interaction potential. Microscopic and macroscopic techniques have been widely used in the past decades (Gharaei, Zanganeh and Wang, 2018). To theoretically study fusion dynamics, a realistic nuclear potential $V_N(r)$ must be defined (Zanganeh, Gharaei and Izadpanah, 2019). Current successful theories describe nuclear interactions in a wide variety of fusion systems, from light to heavy colliding pairs.

Błocki, et al., in 1977, first proposed a phenomenological proximity potential for heavy-ion reactions. The proximity force theorem (Dutt and Puri, 2010a) is used in all proximity potential calculations. Many attempts have used proximity potential formalisms to describe the fusion of two colliding nuclei. The results show that this theoretical method must be improved to interpret the fusion cross-sections at energies below the Coulomb barrier (Gharaei and Sarvari, 2024). This well-known applicable model with simple and accurate formalism has the advantage of adjustable parameters.

The proximity 1977 potential, also known as Prox77 (Umar and Oberacker, 2007), is one of several nuclear proximity potentials used in fusion research. Various proximity potentials have been used to calculate fusion cross-sections, including Prox77, Proximity 1988 (Prox88), Proximity 2000 (Prox00), Proximity 2000DP; and three versions by Bass-Bass 1973 (Bass73), Bass 1977 (Bass77), Bass 1980 (Bass80); three versions by Winther and collaborators – Christensen and Winther 1976 (CW76), Broglia and Winther 1991 (BW91), Aage Winther (AW95); Ngô1975 (Ngô75) and Ngô 1980 (Ngô80); and two versions by Denisov and EDF (Dutt and Puri, 2010b; Thiha and Lwin, 2012). The most recent proximity potential formalisms are the Zhang 2013 and Guo 2013 models (Zhang, Zheng and Qu, 2013; Guo, Zhang and Le, 2013). The key difference between these two theoretical approaches lies in their universal function.

Several factors influence heavy ion fusion cross-sections. Magic numbers, pairing effects, neutron excess, and other nuclear structural factors affect the fusion cross-section. In addition, closed-shell structures in target or projectile nuclei enhance fusion probability (Brown, 2015). For heavy systems, shell effects in the colliding nuclei and Coulomb repulsion expressed as the product of projectile and target atomic numbers (Z_p and Z_t, respectively) affect fusion barrier height (Ikezoe, et al., 2004). We examined the relationship between nuclear fusion cross-sections and several key structural features: Nucleon pairing, magic numbers, closed shells, neutron excess, and deformation.

Knowledge of nuclear structure, and pairing correlations influence the results, is crucial to understanding nuclear

ARO-The Scientific Journal of Koya University
Vol. XIII, No.2(2025), Article ID: ARO.12265. 11 pages
DOI: 10.14500/aro.12265
Received 09 May 2025; Accepted 01 September 2025
Regular research paper; Published: 12 November 2025
†Corresponding author's e-mail: adel.hossien@univsul.edu.iq

http://dx.doi.org/10.14500/aro.12265

collisions. These relationships produce two key outcomes. First, spherical ground-state deformations are stabilized by pairing, thus influencing fusion dynamics. Neutron transfer preceding barrier crossing influences barrier height changes, a process affected by pairing interactions (Sargsyan, et al., 2013).

We selected the best proximity potential versions for fusion cross-section prediction using Chi-square method, comparing them against experimental data, this method can be found in (Ghodsi and Daei-Ataollah, 2016). Preliminary results show the CW76 potential best reproduces experimental fusion cross-section for the studied systems. In addition, we studied how different nuclear structure aspects, including nucleon pairing, magic numbers, closed shells, neutron excess, and deformation, affect fusion cross-sections. This new study provides valuable understanding of the fusion process's dependence on nuclear structure, which has been unstudied with macroscopic potentials.

II. Theoretical Method

We employed a variety of proximity potentials, which include Prox77, Prox80, Prox00, Bass73, Bass77, Bass80, CW76, BW91, AW95, Ngô80, and Denisov DP, to compute the fusion cross-section. Each distinct type of proximity potential was systematically incorporated into the Wong formula to facilitate the computational analyses. Certain nuclear potentials, namely, Prox77, Prox88, Prox00, Bass73, Ngô80, and Denisov DP, do not provide a precise representation of experimental fusion data under specific optimization reaction conditions. As a result, these potentials frequently demonstrate an inability to reliably predict fusion cross-sections; for some reactions, the Chi-square values are either absent or indeterminate, thereby exposing their deficiencies in accurately predicting experimental data.

To identify the best proximity potential, we employed the Chi-square test. Our research indicates that the CW76 potential, developed by Christensen and Winter in 1976, yielded the smallest chi-square value. Next, we calculated the Chi-square value for each cross-section reaction, as illustrated in Fig. 1. In this figure, the Y-axis represents the Chi-square value, while the X-axis shows the product of Z_p and Z_t. The Chi-square values for the CW76 potential range from 0.00527 to 0.796101. Fortunately, we can use the Nelder-Mead Algorithm to enhance the chi-square value of the CW76 potential, bringing it down to between 0 and 0.0484. According to a previous study by Gharaei, et al. (Gharaei, Zanganeh and Wang, 2018), the Chi-square value for the cross-section fusion reaction is:

$$\chi^2 = \frac{1}{m}\sum_{i=1}^{m}\left(\frac{\sigma_i^{exp}\left(E_{c.m}\right)-\sigma_i^{th}(E_{c.m})}{\sigma_i^{exp}\left(E_{c.m}\right)+\sigma_i^{th}(E_{c.m})}\right)^2$$

The variable is the number of experimental data points in each reaction. It's noteworthy that these calculations covered the entire range of bombarding energies. Fig. 1 illustrates how the computed relative errors (χ^2) depend on Z_pZ_t for every proximity potential model. This figure shows how the

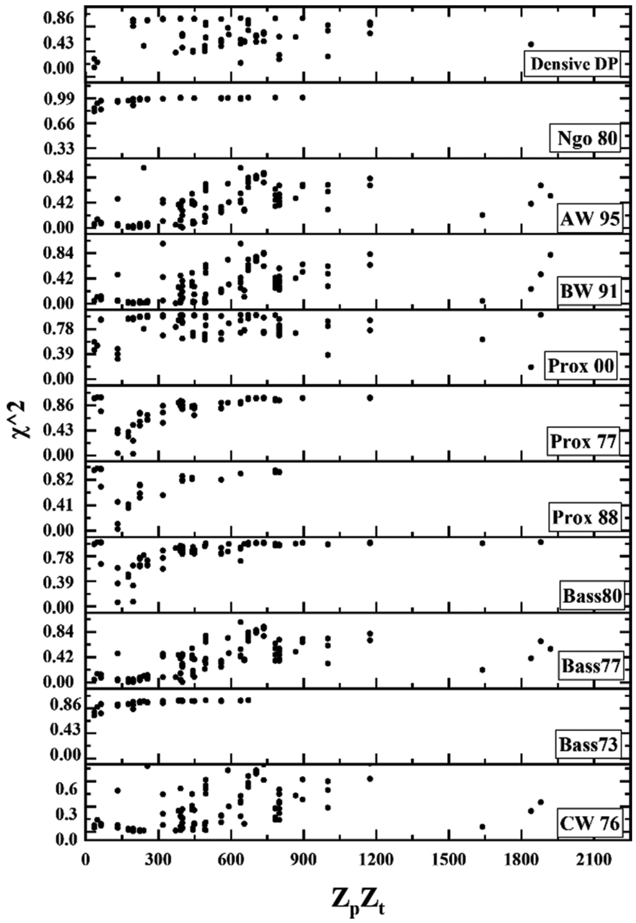

Fig. 1. Chi-square (χ^2) values of fusion cross-sections for various proximity potential models applied to 111 colliding nuclear systems.

theoretical fusion cross-section values differ for 111 fusion reactions across all proximity potentials.

The values of Chi-square of cross-section from CW76 had the following distribution: The χ^2 value showed the following distribution: 50% of the reactions ≤0.2, 22.115% between 0.2 and 0.4, 16.346% between 0.4 and 0.6, and 11.538% between 0.6 and 0.8. After improving the CW76 potential, 77.67% were ≤0.0121; 7.77% were between 0.0121 and 0.0242; 10.68% were between 0.0242 and 0.0363; and 3.88% were between 0.0363 and 0.0484.

A. CW76 Potential and Cross-Section

Using semi-classical arguments and elastic scattering data, Christensen and Wither (Christensen and Winther, 1976; Zhang, et al., 2016; Deb, 2019) determined the nucleus-nucleus interaction potential. The CW76 potential empirical nuclear potential is detailed in (Dutt and Puri, 2010a).

$$V_N^{CW76}\left(r\right) = -50\frac{R_1R_2}{R_1+R_2}\phi(r-R_1-R_2)\ \text{MeV} \quad (1)$$

The projectile and target nuclei radii vary, given as,

$R_i = 1.233A_i^{1/3} - 0.978A_i^{-1/3}$ fm, $(i = 1,2)$

and the universal function becomes.

$$\Phi(s) = exp(-\frac{r - R_1 - R_2}{0.63})$$

The Coulomb potential ($V_C(r)$) and nuclear proximity potential ($V_N(r)$) combine to form the total potential ($V_T(r)$).

$$V_T(r) = V_N(r) + V_C(r), where V_C(r) = (Z_1 Z_2 e^2)/r = \frac{Z_1 Z_2 e^2}{r} \quad (2)$$

The calculated barrier height V_B and its position R_B can be determined using the provided formula and boundary conditions.

$$\left.\frac{dV_T(r)}{dr}\right|_{r=R_B^{th}} = 0; \quad \left.\frac{d^2V_T(r)}{dr^2}\right|_{r=R_B^{th}} \le 0$$

Using Wong's model to calculate the fusion cross-section, which is expressed as:

$$\sigma_{fus} = \frac{\pi}{k^2}\sum_{l=0}^{l_{max}}(2l+1)T_l(E_{c.m}) \quad (3)$$

The wave number, k, is defined as $\sqrt{\frac{2\mu E_{c.m}}{\hbar^2}}$, where μ is the reduced mass and $E_{c.m}$ denotes the center-of-mass energy. The formula above uses l_{max}, the largest partial wave exhibiting a pocket within the interaction potential, and $T_l(E_{c.m})$, representing the penetrating probability, which plays as the energy-dependent barrier penetration factor, which is:

$$T_l(E_{c.m.}) = \left\{1 + exp\left[\frac{2\pi}{\hbar\omega_l}(V_B^{th} - E_{c.m})\right]\right\}^{-1} \quad (4)$$

$\hbar\omega_l$ is the curvature of the inverted parabola. With width and barrier location dependent on orbital angular momentum l, the fusion cross-section becomes,

$$\sigma_{fus}(mb) = \frac{10R_B^{2_{th}}}{2E_{c.m}}\ln\left\{1 + exp\left[\frac{2\pi}{\hbar\omega_l}\left(E_{c.m.} - V_B^{th}\right)\right]\right\} \quad (5)$$

when $E_{c.m} >> V_B^{th}$, the formula simplifies to the used sharp cutoff formula.

$$\sigma_{fus}(mb) = 10\pi R_B^{th^2}\left(1 - \frac{V_B^{th}}{E_{c.m.}}\right) \quad (6)$$

Whereas for $E_{c.m} << V_B^{th}$, the formula (5) transforms, and the parameter of is the curvature of the inverted parabola. When is independent of l, it is written as $\hbar\omega_l$ $(\hbar\omega_0 \simeq \hbar\omega_B)$. A description of the very low-energy fusion cross-section behavior near and below the Coulomb barrier can be obtained.

$$\hbar\omega_B = \left[\frac{-\hbar^2}{\mu}\left.\frac{d^2V_T(r)}{dr^2}\right|_{r=R_B^{th}}\right]^{1/2}$$

With width and barrier location dependent the fusion cross-section becomes,

$$\sigma_{fus}(mb) = \frac{10 R_B^{th^2}\hbar\omega_0}{2E_{c.m.}}exp\left[\frac{2\pi}{\hbar\omega_0}(E_{c.m.} - V_B^{th})\right] \quad (7)$$

we used the above equation to calculate fusion cross-section.

All numerical computations (1)–(7) were performed using a Python script. The fusion parameters, R_B^{th}, V_B^{th}, and , were calculated using the CW76 potential and then later utilized in Wong's formula (6) and (7). Equations (6) and (7) were solved numerically using Newton's method. In addition, we improved CW76 potential based on the fitted parameters (R_B^{th}, V_B^{th}, and $\hbar\omega_B$) according to the experimental fusion cross-section data. For the fitting process, we used the Nelder-Mead Algorithm (Mathews and Fink, 2004; Nelder and Mead, 1965; Yulianto and Zu'ud, 2018).

B. Statistical Methods

It can be challenging to identify which reaction has a higher cross-section because the estimated and observed fusion cross-sections in some reactions appear to overlap in linear and logarithmic plots. To address this issue, we used statistical analysis to compare the fusion cross-sections of the different procedures. In particular, we employed a statistical test that concentrated on the mean difference to ascertain the variance in fusion cross-sections across the reactions. Accurate fusion cross-section data was analyzed using two statistical techniques. Tukey's multiple comparisons and Welch's correction are used in the unpaired t-test (Abdi and Williams, 2010). The means of two calculated reactions were compared using Welch's t-test.

The Welch's t-test was used to compute Table I, which tabulated the mean difference value (Column B minus Column A) and its standard error mean (SEM). According to previous work (Neideen and Brasel, 2007), the t-test computes the test statistic using the mean, standard deviation, and number of samples. Mean comparison is the primary focus of many conventional statistical methods. Welch's t-test, which is utilized for certain reactions as indicated in Table I, is usually selected when the variances are not equal (Lu and Yuan, 2010).

$$t_w = \frac{\overline{y_1} - \overline{y_2}}{\sqrt{\frac{s_1^2}{n_1} + \frac{s_2^2}{n_2}}} \quad (8)$$

The generalized form of the used variables is written as:

$$\overline{y_j} = \frac{1}{n_j}\sum_{i=1}^{n_j} y_{ij} \text{ and } s_j^2 = \frac{1}{n_j - 1}\sum_{i=1}^{n_j}(y_{ij} - \overline{y_j})^2 \quad (9)$$

Where $\overline{y_J}$ is mean of sample j where (j = 1,2), is variance of sample of group j, and n_j is sample size of group j.

As the name implies, ANOVA is an acronym for analysis of variance, and a one-way ANOVA was used

TABLE I
Fusion Cross-Section Mean Values Between Fusion Systems, Using Unpaired T-Tests with Welch's Correction

Column A	Column B	Mean of column A (mb)	Mean of column B (mb)	Mean difference ((B–A)±SEM) (mb)
$^{16}O+^{58}Ni$	$^{16}O+^{62}Ni$	334.40	313.30	−21.10±3.79
$^{16}O+^{148}Sm$	$^{16}O+^{154}Sm$	77.27	114.10	37.13±13.41
$^{12}C+^{46}Ti$	$^{12}C+^{50}Ti$	548.40	449.20	−99.20±34.96
$^{28}Si+^{28}Si$	$^{28}Si+^{30}Si$	68.79	71.43	2.64±4.23
$^{16}O+^{46}Ti$	$^{16}O+^{50}Ti$	354.40	284.60	−69.85±193.50
$^{16}O+^{112}Sn$	$^{16}O+^{116}Sn$	208.00	222.60	14.55±42.87

to analyze cross-sectional variations across three or more fusion processes (Kim, 2017). When comparing means value pairwise, the honestly significant differences (HSDs) methodology also known as Tukey's HSD includes the error rate at the predetermined α threshold (Tukey, 1953; Brown, 2005) (Ostertagova and Ostertag, 2013). To determine the maximum mean cross-section value in Table II, Tukey's HSD computed the mean differences between the means of each fusion system.

$$\text{HSD} = q_{\alpha,A}\sqrt{\frac{MS_{S(A)}}{S}} \tag{10}$$

The difference in mean sample is equal to $\overline{X_1} - \overline{X_2}$

$$\overline{X_j} = \frac{1}{n_j}\sum_{i=1}^{n_j} X_{ij} \tag{11}$$

$$\text{SE} = \sqrt{\frac{MSW}{2}\left(\frac{1}{n_1}+\frac{1}{n_2}\right)} \tag{12}$$

Where SE is the standard error of the difference between two means, and the formula for the Tukey test statistic is:

$$q = \frac{\overline{X_1} - \overline{X_2}}{\sqrt{\frac{MSW}{2}\left(\frac{1}{n_1}+\frac{1}{n_2}\right)}} \tag{13}$$

Where *MSW* is the mean square error from the previously calculated ANOVA, *S* is the number of observations per group, *X* is the group means, and *n* is the number of observations in each relevant group (The groupings are thought to be the same size) (Abdi and Williams, 2010).

III. Results and Discussion

We used the chi-square method to choose the optimal CW76 proximity potential from various types, based on how well it reproduces experimental fusion cross-section data. The CW76 potential was used in this study to reproduce fusion reactions, and the barrier parameters of both the CW76 and the improved CW76 potentials are shown in Table III. Calculating reaction cross-sections reveals physical phenomena, including shell effects, pairing, neutron excess, magic numbers, and nuclear deformation. We used statistical variance analysis to determine the differences in enhanced fusion cross-sections between two systems using the same projectile but different targets (either element nuclei or their isotopes). The cross-section results are thus organized by projectile nuclei.

TABLE II
Tukey's Multiple Comparisons Test is Used to Compare the Mean Value of Fusion Cross-Sections of Reaction Systems

Reaction 1	Reaction 2	Mean reaction 1 (mb)	Mean reaction 2 (mb)	Mean difference (mb) (mean reaction 2−mean reaction 1)
$^{12}C+^{182}W$	$^{12}C+^{184}W$	454.30	585.50	131.10
$^{12}C+^{182}W$	$^{12}C+^{186}W$	454.30	681.10	226.80
$^{12}C+^{184}W$	$^{12}C+^{186}W$	585.50	681.10	95.64
$^{12}C+^{204}Pb$	$^{12}C+^{206}Pb$	463.30	428.50	34.73
$^{12}C+^{204}Pb$	$^{12}C+^{208}Pb$	463.30	449.70	−13.56
$^{12}C+^{206}Pb$	$^{12}C+^{208}Pb$	428.50	449.70	21.17
$^{28}Si+^{58}Ni$	$^{28}Si+^{62}Ni$	32.91	47.56	14.65
$^{28}Si+^{58}Ni$	$^{28}Si+^{64}Ni$	32.91	55.17	22.26
$^{28}Si+^{62}Ni$	$^{28}Si+^{64}Ni$	47.56	55.17	7.61
$^{28}Si+^{90}Zr$	$^{28}Si+^{92}Zr$	417.10	176.80	−242.30
$^{28}Si+^{90}Zr$	$^{28}Si+^{94}Zr$	417.10	198.80	−218.30
$^{28}Si+^{92}Zr$	$^{28}Si+^{94}Zr$	176.80	198.80	22.00
$^{58}Ni+^{58}Ni$	$^{58}Ni+^{60}Ni$	36.84	100.30	63.46
$^{58}Ni+^{58}Ni$	$^{58}Ni+^{64}Ni$	36.84	95.03	58.19
$^{58}Ni+^{60}Ni$	$^{58}Ni+^{64}Ni$	100.30	95.03	−5.27

A. ^{16}O Projectile Nucleus

Anomalies found during the computation of the fusing of double magic oxygen projectiles with titanium isotopes, ^{46}Ti and ^{50}Ti, are depicted in Fig. 2a and b. Each figure has its own set of specifications. In contrast to Fig. 2b, which employs a logarithmic scale, Fig. 2a uses a linear scale. The other cross-section values fall into the same category. Closed-shell nuclei in the ^{46}Ti target are not composed of either proton or neutron configurations. On the other hand, the neutron magic number of the target (^{50}Ti) is 28. As shown in Fig. 2a, the enhanced CW76 potential (Imp_CW76), which incorporates Wong's formula (Eq. 7), generally reproduces experimental data more accurately than the original CW76 potential.

At high energies, the Imp_CW76 potential offers better accuracy by resolving inconsistencies between CW76 data and experimental fusion cross-section measurements for $^{16}O + ^{50}Ti$, as shown in Fig. 2a.

The calculated findings of the fusion cross-section at low-energy levels for, $^{16}O + ^{46}Ti$ with $^{16}O + ^{50}Ti$, differ slightly in Fig. 2b. We employed mean difference approaches to identify the minor differences (overlap). Table I and Fig. 3a show that the mean difference in cross-section values between the $^{16}O + ^{50}Ti$ and $^{16}O + ^{46}Ti$ systems is −69.85 ± 193.50 mb. This indicates that the mean cross-section value of the $^{16}O + ^{46}Ti$ system is greater than that of the $^{16}O + ^{50}Ti$ system. Surprisingly, the neutron magic number effect resulted in a smaller fusion cross-section, which counteracted the excess of neutrons, thereby enhancing the cross-section.

The shell effect also arises in the new fusion system. The computed fusion cross-section for, $^{16}O + ^{62}Ni$ is smaller than that for, $^{16}O + ^{58}Ni$ in the high energy range, as shown in Fig. 2c and d. The systems' computed fusion cross-section agrees better with experimental data. Each target has a different structure, which accounts for this small discrepancy. While ^{62}Ni possesses both a neutron excess and an occupied sub-shell state, ^{58}Ni has only one neutron pair and no occupied sub-shell $1f_{\frac{5}{2}}$ state. For light-medium mass regions, this identification employs a fixed-target single-particle configuration, as explained in (Brown, 2015; Hagino and Maeno, 2020; Recchia, et al., 2013). According to articles like (Brown, Derevianko and Flambaum, 2009), this arrangement is recommended for medium-heavy mass zones. The closed sub-shell effect can be estimated to have cancelled out the cross-section enhancement. The improve CW76 calculation cross-section mean difference between $^{16}O + ^{58}Ni$ and $^{16}O + ^{62}Ni$ is −21.10 ± 3.79 mb (Fig. 3b and Table I).

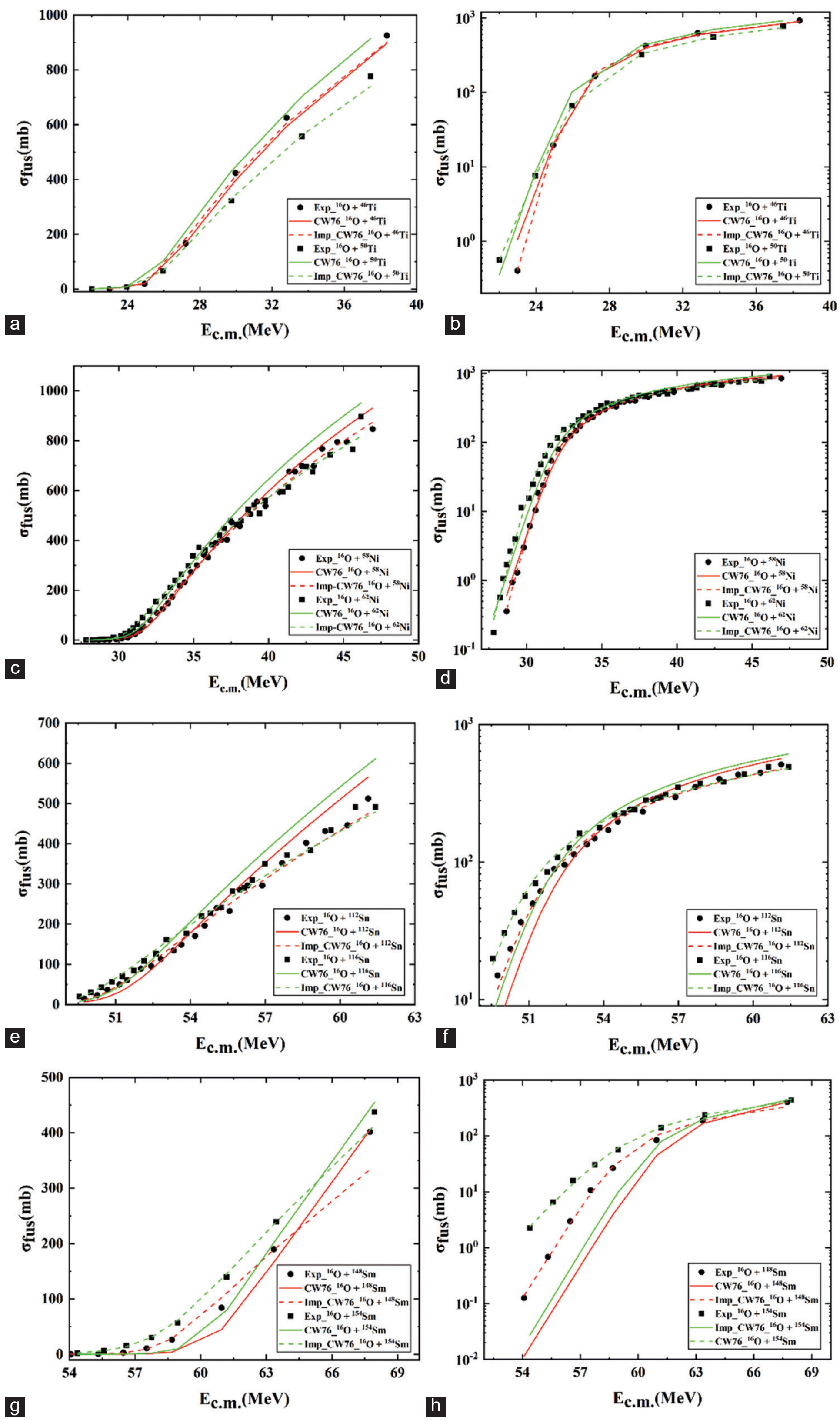

Fig. 2. The calculate and experiment cross-section of the projectile oxygen-16 fused with (a, b) Titanium isotopes ^{46}Ti and ^{50}Ti, (c, d) Nickle isotopes ^{58}Ni and ^{62}Ni, (e, f) Tin isotopes ^{112}Sn and ^{116}Sn, and (g, h) Samarium even isotopes ^{148}Sm and ^{154}Sm. The chosen system's experimental data are from (Denisov and Sedykh, 2019; Gharaei, Hadikhani and Zanganeh, 2019).

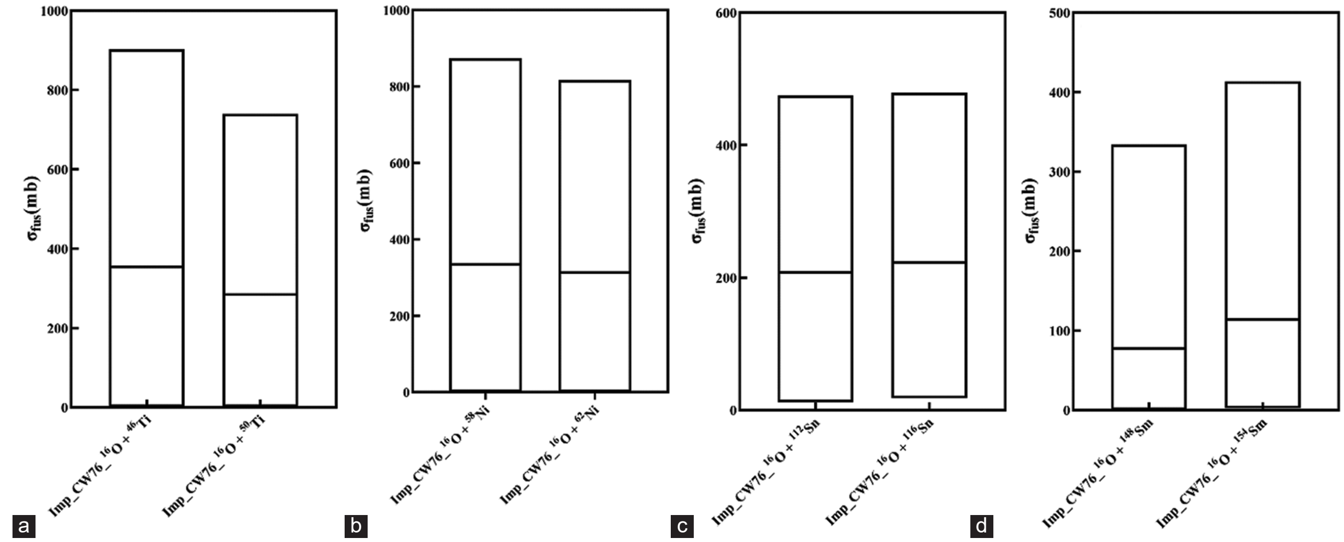

Fig. 3. Calculated fusion cross-section value and mean value for the reaction of ^{16}O with various target isotopes (a) Titanium isotopes ^{46}Ti and ^{50}Ti, (b) Nickle isotopes ^{58}Ni and ^{62}Ni, (c) Tin isotopes ^{112}Sn and ^{116}Sn, and (d) Samarium even isotopes ^{148}Sm and ^{154}Sm. The line within each bar shows the mean value of the calculated fusion cross-section.

This small mean cross-section value of ^{16}O + ^{62}Ni is further supported by the closed-shell property of ^{62}Ni.

Figs. 2e and f demonstrate that the calculated Imp_CW76 cross-section agree well with experimental results. In addition, the reaction cross-section for ^{16}O + ^{116}Sn is larger than that of ^{16}O + ^{112}Sn. This is because to the difference in neutron pairs; however, although ^{112}Sn has two neutron pairs, ^{116}Sn has just one. A small estimated mean difference with a value of (14.55 ± 42.87) mb was shown in Fig. 3c and is shown in Table I. The pairing effect is responsible for this low value, even though it surpasses the neutron target, ^{116}Sn.

Figs. 2g and h shows that the calculated Imp_CW76 cross-section reactions are coincide the experimental data. The calculated fusion cross-section of ^{16}O + ^{154}Sm has a greater value than that ^{16}O + ^{148}Sm. ^{154}Sm targets neutrons in the $1h_{\frac{9}{2}}$ state, target neutrons exhibit an excess neutron property in comparison to ^{148}Sm. The computed fusion cross-section mean difference for the reactions ^{16}O + ^{148}Sm and ^{16}O + ^{154}Sm is (37.13 ± 13.41) mb, as shown in Table I and also in Fig. 3d. This result demonstrated that the influence of the neutron excess decreased with the development of a sub-shell, resulting in a small mean variation in the cross-section.

B. ^{12}C Projectile Nucleus

Closed-shell ^{12}C nuclei, possessing neutron-proton symmetry, reacted through fusion with ^{46}Ti and ^{50}Ti. Fig. 4a and b shows that the calculated Imp_CW76 fusion cross-section among these reactions is close to experimental results. The ^{12}C + ^{46}Ti enhanced the value more than for ^{12}C + ^{50}Ti especially in the high-energy range. Table I provides further evidence of a (−99.20 ± 34.96) mb mean difference cross-section for ^{12}C + ^{46}Ti and ^{12}C + ^{50}Ti, as illustrated in Fig. 5a.

Next, the study focuses on asymmetric fusion reactions between ^{12}C and the tungsten isotopes ^{182}W, ^{184}W, and ^{186}W as shown in Fig. 4(c- linear scale) and Fig. 4(d- logarithmic scale). The neutron configurations are as follows: one neutron pair in the $3p_{\frac{3}{2}}$ state for ^{182}W, and occupying the $3p_{\frac{3}{2}}$ and $3p_{\frac{1}{2}}$ subshells for ^{184}W and ^{186}W, respectively (Brown, Derevianko and Flambaum, 2009). Fig. 4 (c, d) shows that the calculated cross-section closely reproduces the experimental data, except beyond 64 MeV. These results, more clearly shown in Fig. 5b, highlight that the excess neutron and sub-shell effect within the ^{186}W target are key to the enhanced ^{12}C + ^{186}W cross-section compared to ^{12}C + ^{182}W. These results are sustained numerically by Table II, where the Imp_CW76 calculated data recorded the largest cross-section mean difference between ^{12}C + ^{182}W and ^{12}C + ^{186}W to be 226.80 mb.

Extreme asymmetry fusion is observed in fusion reactions between ^{12}C projectiles and the Pb target isotopes ^{204}Pb, ^{206}Pb, and ^{208}Pb. Fig. 4e and f presents the experimental data reproduced by the Imp_CW76 calculated cross-section, except for the 80–85 MeV energy range, specifically for ^{12}C + ^{204}Pb. The influence of nuclear structure on these reactions is not easily discernible in Fig. 4e and f. Therefore, a mean cross-section analysis gives a more precise understanding. Fig. 5c displays the small mean difference of −13.56 mb between ^{12}C + ^{204}Pb and ^{12}C + ^{208}Pb, as tabulated in Table II. This is peculiar because the double magic number of the ^{208}Pb target slightly lowered the fusion cross-section. However, it contains four extra neutrons compared to the ^{204}Pb target.

C. ^{28}Si Projectile Nucleus

The symmetric and semi-symmetric fusion reactions of the closed shell ^{28}Si projectile with ^{28}Si and ^{30}Si targets are shown in Fig. 6a and b. The Imp_CW76 calculated fusion cross-sections coincided with the experimental data. The fusion of ^{28}Si + ^{30}Si shows a higher calculated result compared to the symmetric ^{28}Si + ^{28}Si reaction. ^{28}Si and ^{30}Si, while both closed-shell nuclei, differ significantly in that

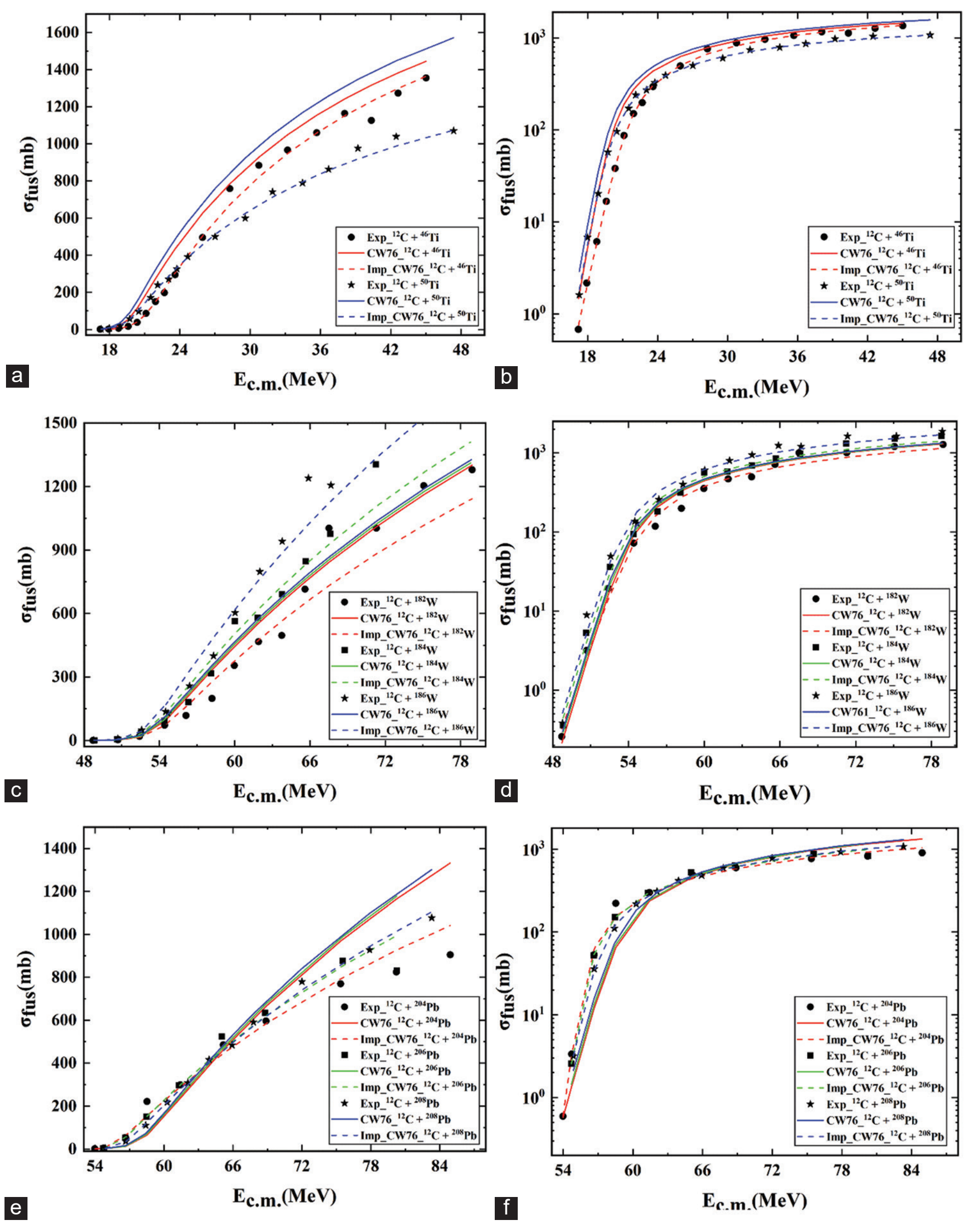

Fig. 4. The calculate and experimental fusion cross-section of the projectile ^{12}C fused with (a and b) Titanium isotopes ^{46}Ti and ^{50}Ti, (c and d) Tungsten isotopes ^{182}W, ^{184}W, and ^{186}W, (e and f) Lead isotopes ^{204}Pb, ^{206}Pb, and ^{208}Pb. Experimental data for chosen systems came from (Denisov and Sedykh, 2019; Gharaei, Hadikhani and Zanganeh, 2019).

^{30}Si's neutrons occupy the $(2s_{1/2})$ ground state. Another target difference is that the combined ^{28}Si + ^{28}Si nucleus's oblate shape (Denisov and Pilipenko, 2010) leads to a lower fusion cross-section than ^{28}Si + ^{30}Si because the projectile is oblate and the target is spherical. However, the ^{30}Si target's spherical nature and a single neutron pair in its $2s_{1/2}$ state raised the fusion cross-section, with neutron transfer further boosting it (Manjunatha, et al., 2023; Othman, Hussein and Taqi, 2023). Fig. 7a displays a small mean difference (2.64 ± 4.23) mb between ^{28}Si + ^{28}Si and ^{28}Si + ^{30}Si calculated cross-sections, as shown in Table I. Because both contradicting properties, spherical and extended neutron, are collected in the same target ^{30}Si.

Fig. 6c and d illustrates fusion reactions involving either a rich neutron pair or neutron transfer. The Imp_CW76 calculated fusion cross-sections for ^{28}Si + $^{58,62,64}Ni$ agree with experimental data, except in the 58 MeV energy range. Table II and Fig. 7b show that the calculated cross-section mean difference between ^{28}Si + ^{58}Ni and ^{28}Si + ^{64}Ni is 22.26 mb. The reason is that the ^{64}Ni neutron excess enhanced the cross-section.

Another asymmetry fusion reaction uses ^{28}Si projectiles and ^{90}Zr, ^{92}Zr and ^{94}Zr zirconium target isotopes, the reaction ^{28}Si + ^{90}Zr has highest fusion cross-section especially in the 75–95 energy range. Fig. 6e and f shows that the Imp_CW76 calculated fusion cross-sections somewhat under-predict the experimental data. Fig. 7c and Table II illustrate an anomalous

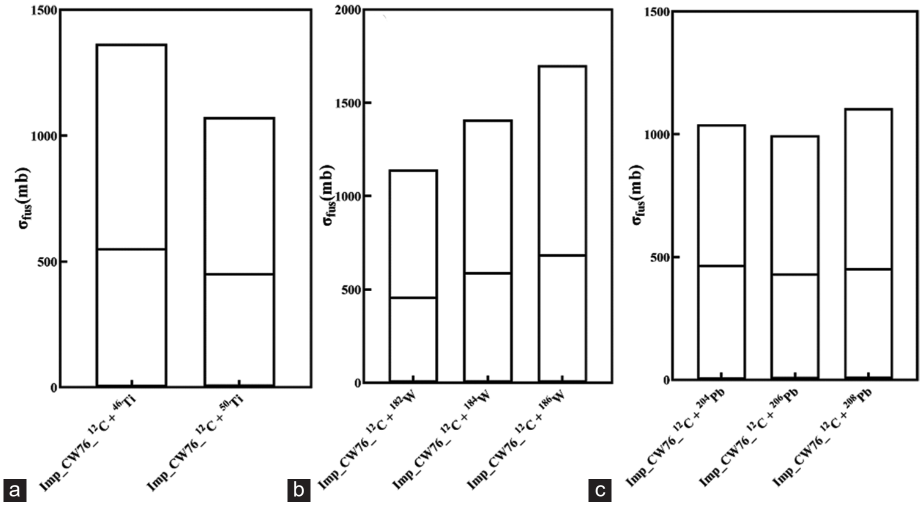

Fig. 5. Calculated fusion cross-section value and mean value for the reaction of ^{12}C with various target isotopes (a) Titanium isotopes ^{46}Ti and ^{50}Ti, (b) Tungsten isotopes ^{182}W, ^{184}W, and ^{186}W, (c) Lead isotopes ^{204}Pb, ^{206}Pb, and ^{208}Pb.

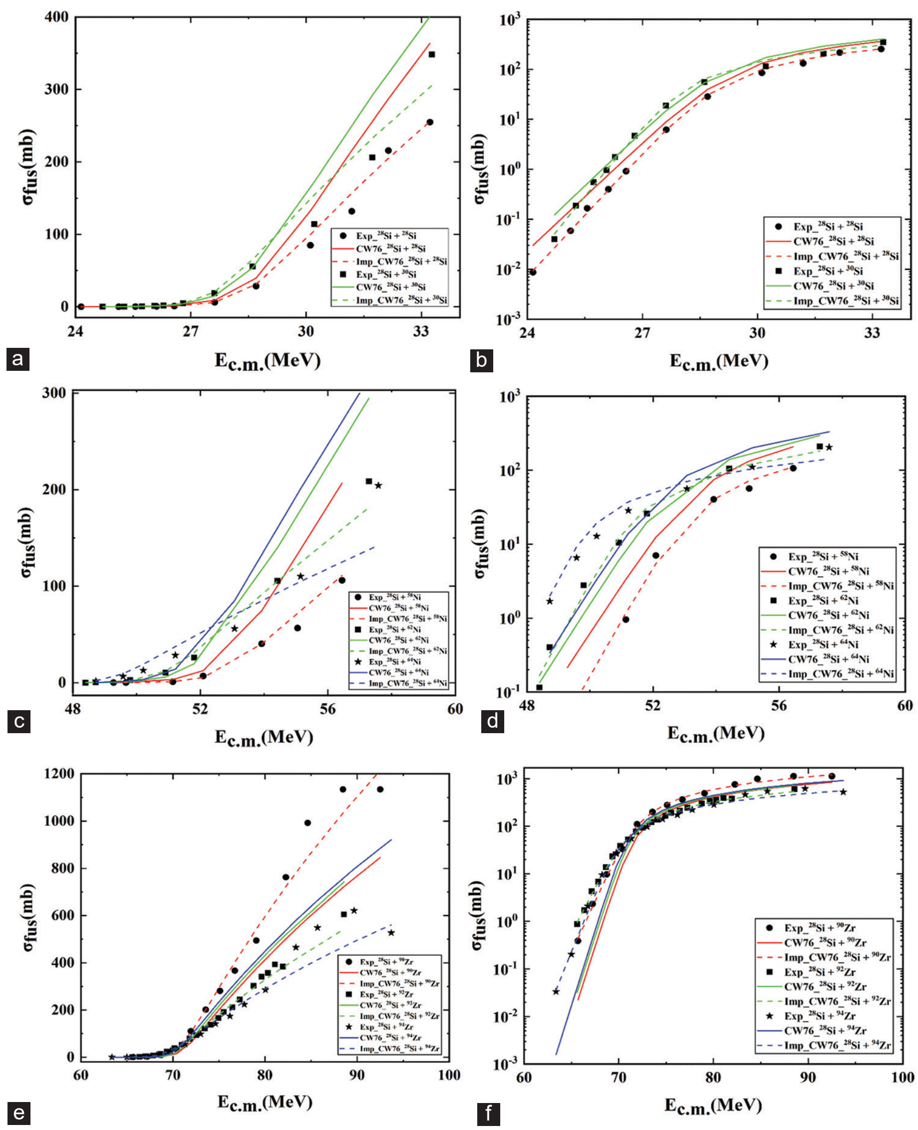

Fig. 6. The calculate and experiment cross-section of the projectile ^{28}Si fused with (a and b) Silicon isotopes ^{28}Si and ^{30}Si, (c and d) Nickel isotopes ^{58}Ni, ^{62}Ni, and ^{64}Ni, (e and f) Zirconium isotopes ^{90}Zr, ^{92}Zr, and ^{94}Zr. Experimental data for chosen systems came from (Denisov and Sedykh, 2019; Gharaei, Hadikhani and Zanganeh, 2019).

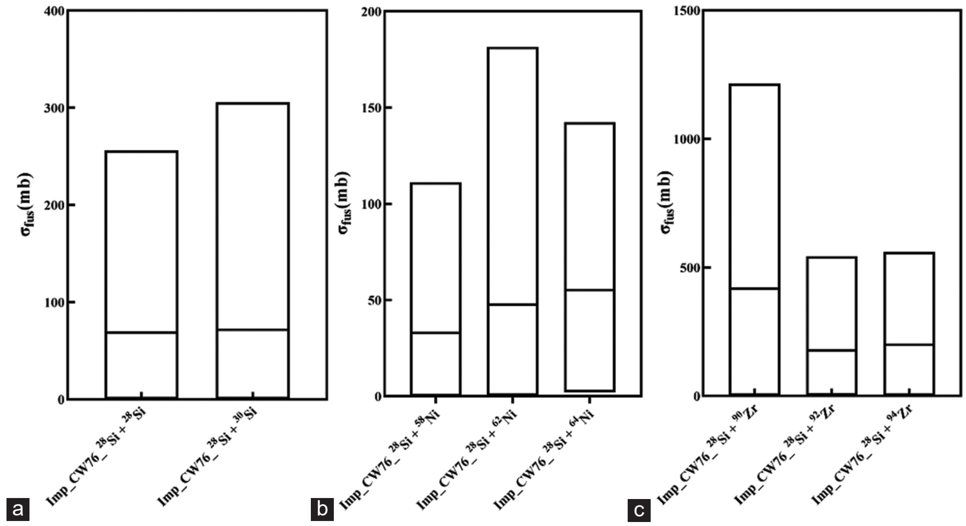

Fig. 7. Calculated fusion cross-section value and mean value for the reaction of ^{28}Si with various target isotopes (a) Silicon isotopes ^{28}Si and ^{30}Si, (b) Nickel isotopes ^{58}Ni, ^{62}Ni, and ^{64}Ni, and (c) Zirconium isotopes ^{90}Zr, ^{92}Zr, and ^{94}Zr.

TABLE III
THE FUSION BARRIER HEIGHTS V_B (IN MEV) AND POSITIONS R_B (IN FM) AND THE CURVATURE $\hbar\omega_B$ (IN MEV)

Reaction	Improved CW 76 potential			CW 76 potential		
	R_B	V_B	$\hbar\omega_B$	R_B	V_B	$\hbar\omega_B$
^{16}O+^{46}Ti	9.190922	25.319404	2.987033	9.247181	25.546388	3.770844
^{16}O+^{50}Ti	8.598335	25.520146	4.511296	9.408749	25.139222	3.695493
^{16}O+^{58}Ni	9.120545	31.246414	3.339573	9.529376	31.619062	4.079494
^{16}O+^{62}Ni	8.738370	30.447063	3.235988	9.665938	31.203519	3.936642
^{16}O+^{112}Sn	9.307705	50.458518	4.422943	10.567145	51.271570	4.575866
^{16}O+^{116}Sn	8.961275	49.756989	4.058019	10.652038	50.888650	4.544718
^{16}O+^{148}Sm	8.789926	58.418534	4.926418	11.110830	60.653333	4.880284
^{16}O+^{154}Sm	9.573062	58.195344	7.410088	11.214582	60.125615	4.853278
^{28}Si+^{28}Si	7.531741	28.445801	3.248914	9.175906	28.654087	3.692511
^{28}Si+^{30}Si	7.567809	27.622500	2.834262	9.295111	28.313356	3.623869
^{28}Si+^{58}Ni	7.290250	52.684161	3.560797	10.031191	52.751433	4.166359
^{28}Si+^{62}Ni	7.197916	50.896562	3.356839	10.167715	52.089959	4.064009
^{28}Si+^{64}Ni	5.604451	49.273735	2.610209	10.233480	51.777174	3.955034
^{28}Si+^{90}Zr	12.818665	70.741482	6.140282	10.718836	70.827866	4.423911
^{28}Si+^{92}Zr	9.001324	69.685624	6.791096	10.768881	70.519173	4.394901
^{28}Si+^{94}Zr	8.259465	69.190337	5.451221	10.818122	70.218046	4.249320
^{12}C+^{46}Ti	8.982249	20.780712	4.524896	9.025324	19.595488	3.691562
^{12}C+^{50}Ti	7.611167	19.412007	3.785775	9.186829	19.276396	3.650554
^{12}C+^{182}W	10.661443	53.682271	5.838090	11.313356	53.379941	5.088369
^{12}C+^{184}W	11.704385	52.971077	5.127369	11.343460	53.246609	5.056939
^{12}C+^{186}W	12.803812	52.807743	4.974638	11.373327	53.114982	4.992695
^{12}C+^{204}Pb	9.781672	55.495077	2.623839	11.559605	57.963409	5.294642
^{12}C+^{206}Pb	10.191373	55.783516	2.924071	11.587349	57.832606	5.233726
^{12}C+^{208}Pb	10.441434	56.419614	3.949549	11.614898	57.703302	5.265551
^{58}Ni+^{58}Ni	5.899646	95.558527	3.226730	10.889831	97.697698	4.312976
^{58}Ni+^{60}Ni	7.562228	96.068957	5.502213	10.958807	97.120297	4.282280
^{58}Ni+^{64}Ni	7.943106	94.938123	6.356954	11.091686	96.026907	4.138919

effect, with −218.30 mb mean difference observed in the calculated cross-section between ^{28}Si + ^{90}Zr and ^{28}Si + ^{94}Zr.

D. ^{58}Ni Projectile Nucleus

The fusion cross-sections of three Nickel-based reactions are investigated in this study. ^{58}Ni + ^{58}Ni, ^{58}Ni + ^{60}Ni and

TABLE IV
CALCULATION OF MEAN VALUES IN (MB) FOR THE DIFFERENT PROJECTILES

Target	Projectile comparison			
	^{12}C	^{16}O	^{28}Si	^{58}Ni
^{28}Si			68.79	
^{30}Si			71.43	
^{46}Ti	548.40	354.40		
^{50}Ti	449.20	284.60		
^{58}Ni		334.40	32.91	36.84
^{60}Ni				100.30
^{62}Ni		313.30	47.56	
^{64}Ni			55.17	95.03
^{90}Zr			417.10	
^{92}Zr			176.80	
^{94}Zr			198.80	
^{112}Sn		208.0		
^{116}Sn		222.60		
^{148}Sm		77.27		
^{154}Sm		114.10		
^{182}W	454.30			
^{184}W	585.50			
^{186}W	681.10			
^{204}Pb	463.30			
^{206}Pb	428.50			
^{208}Pb	449.70			

^{58}Ni + ^{64}Ni were analyzed, as shown in Fig. 8a and b. Fig. 8a shows that the Imp_CW76 calculated fusion cross-sections (^{58}Ni + ^{58,60,64}Ni) agree well with experimental data, aside from the 102–114 MeV energy range.

Among the reactions, the cross-section mean value for ^{58}Ni + ^{60}Ni is the highest (Fig. 9). Table II further reveals that the largest mean difference 63.46 mb in calculated cross-sections is between ^{58}Ni + ^{58}Ni and ^{58}Ni + ^{60}Ni. This is due to neutron-rich target isotopes allowing for easier fusion between colliding nuclei (Gautam, Kaur and Sharma, 2015). In addition, a key distinction lies in the internal structure of nickel isotopes, with ^{60}Ni showing more deformability than ^{58}Ni, leading to greater neutron transfer.

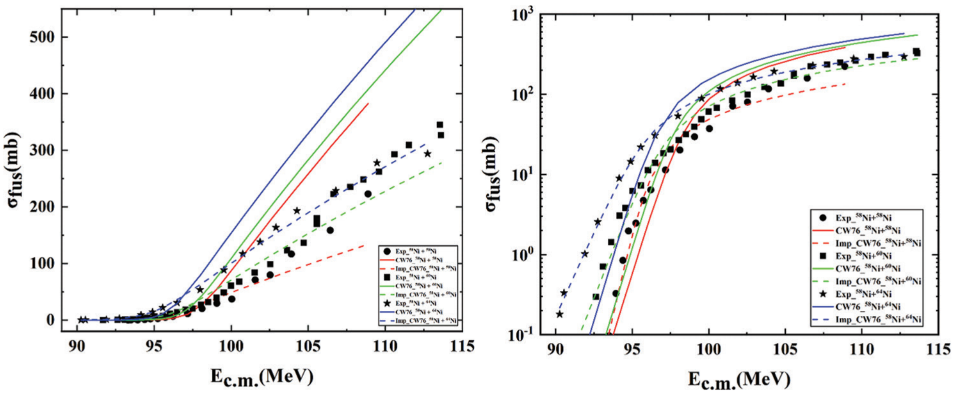

Fig. 8. The calculate and experiment cross-section of the Nickel projectile ^{58}Ni fused with its isotopes ^{58}Ni, ^{60}Ni, and ^{64}Ni targets. Experimental data for chosen systems came from (Denisov and Sedykh, 2019; Mişicu and Esbensen, 2007).

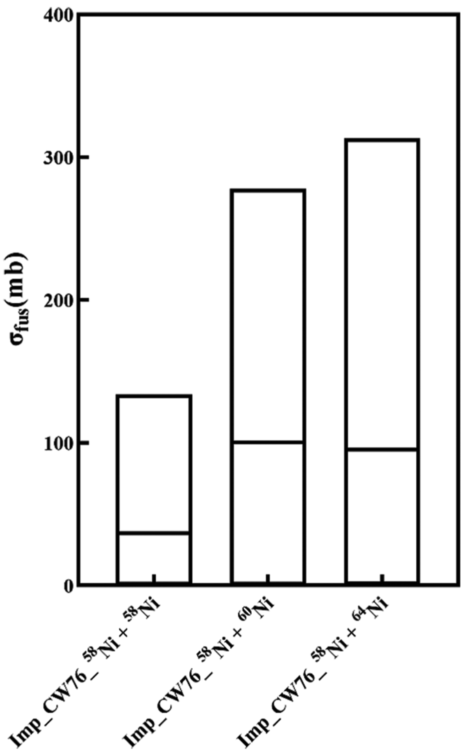

Fig. 9. Calculated fusion cross-section value and mean value for the reaction of ^{58}Ni fused with its isotopes ^{58}Ni, ^{60}Ni, and ^{64}Ni targets.

IV. Conclusion and Summery

This study presents calculations of fusion cross-sections for various systems using the Wong formula and the CW76 potential. The CW76 proximity potential and its improved version allowed for a rapid assessment of 111 fusion systems to identify analogs and relationships and predict anomalies through cross-section Chi-square. Our findings show that Imp_CW76 is crucial for reproducing much of the experimental fusion reaction data. This potential consequently optimally guides practical researchers to make better predictions. In addition, we investigated how nuclear properties such as magic numbers, shell effects, nuclear shapes, and neutron excess influence fusion cross-sections (Figs. 2-4(a, b, e, f), 5a and c, 6a-f, 7 and 8).

Our data show that shell effects influence fusion cross-sections. The increased mean difference is because the ^{90}Zr target's neutron magic number surpasses the ^{94}Zr target's neutron excess when each is fused separately with the same ^{28}Si projectile (Table II). Despite target ^{50}Ti having a higher neutron number than ^{46}Ti, ^{12}C + ^{46}Ti has a greater fusion cross-section than ^{12}C + ^{50}Ti. This pattern repeats for the projectile ^{16}O that fused with each of ^{46}Ti and ^{50}Ti targets. A surprising phenomenon is that shell effects and the magic number of ^{50}Ti mitigate the neutron excess effect in specific fusion reactions, also including ^{16}O + ^{62}Ni (vs. ^{16}O + ^{58}Ni) and ^{12}C + ^{208}Pb (vs. ^{12}C + ^{204}Pb).

The fusion of ^{28}Si projectiles with ^{30}Si (spherical, $2s_{1/2}$ subshell closed) target reveals a higher fusion cross-section compared to the ^{28}Si target. The neutron excess in ^{116}Sn overcame the pairing effect in the ^{112}Sn target as the ^{112}Sn target fused with the ^{16}O projectile.

Conversely, a greater fusion cross-section enhancement is observed in titanium target isotopes (^{46}Ti, ^{50}Ti) when fused with the closed-shell projectile ^{12}C, unlike when fused with the double-magic projectile ^{16}O. Table IV shows that the fusion cross-section of ^{58}Ni and ^{62}Ni isotopes fused with ^{16}O has a greater mean value of fusion cross-section than that of ^{28}Si and ^{58}Ni. We conclude that, as the projectile mass number increases, the fusion cross-section decreases for the same target.

V. Acknowledgments

The authors acknowledge the support for this study from the Department of Physics, College of Science, University of Sulaimani, Sulaymaniyah City, Iraq.

References

Abdi, H., and Williams, L.J., 2010. Tukey's honestly significant difference (HSD) test. In: Salkind, N.J., Ed. *Encyclopedia of Research Design.* Sage, Thousand Oaks, CA, pp.1-5.

Błocki, J., Randrup, J., ŚwiąTecki, W.J., and Tsang, C.F., 1977. Proximity forces. *Annals of Physics,* 105(2), pp.427-462.

Brown, A.M., 2005. A new software for carrying out one-way ANOVA post hoc tests. *Computer Methods and Programs in Biomedicine,* 79(1), pp.89-95.

Brown, B.A., 2015. The nuclear pairing gap - how low can it go? *Journal of Physics: Conference Series,* 580(1), p.012016.

Brown, B.A., Derevianko, A., and Flambaum, V.V., 2009. Calculations of the neutron skin and its effect in atomic parity violation. *Physical Review C,* 79(3), p.035501.

Christensen, P.R., and Winther, A., 1976. The evidence of the ion-ion potentials from heavy ion elastic scattering. *Physics Letters B,* 65(1), pp.19-22.

Deb, N., 2019. Behaviour of nuclear bass and winther potentials towards the fusion sub-barrier cross section of $^{16}O+^{58,62}Ni$. *Journal of Applied and Fundamental Sciences,* 5(2), p.49.

Denisov, V.Y., and Pilipenko, N.A., 2010. Interaction and fusion of deformed nuclei. *Physics of Atomic Nuclei,* 73(7), pp.1152-1163.

Denisov, V.Y., and Sedykh, I.Y., 2019. Empirical relations for the fusion cross sections of heavy ions. *The European Physical Journal A,* 55(9), p.153.

Dutt, I., and Puri, R.K., 2010a. Analytical parametrization of fusion barriers using proximity potentials. *Physical Review C,* 81(6), p.064608.

Dutt, I., and Puri, R.K., 2010b. Systematic study of the fusion barriers using different proximity-type potentials for N=Z colliding nuclei: New extensions. *Physical Review C,* 81(4), p.044615.

Gautam, M., Kaur, A., and Sharma, M., 2015. *Fusion Dynamics of* + *Reaction Using Static and Energy Dependent Woods-Saxon Potential,* Proceedings of the DAE-BRNS Symposium on Nuclear Physics. Vol. 60. Bhabha Atomic Research Centre.

Gharaei, R., and Sarvari, E., 2024. Investigating the impact of the universal function of the nuclear proximity potential in heavy-ion fusion cross sections. *Communications in Theoretical Physics,* 76(5), p.055301.

Gharaei, R., Hadikhani, A., and Zanganeh, V., 2019. An explanation for the anomaly problem of diffuseness parameter of the nucleus-nucleus potential in heavy-ion fusion reactions: A possible thermal solution. *Nuclear Physics A,* 990, pp.47-63.

Gharaei, R., Zanganeh, V., and Wang, N., 2018. Systematic study of proximity potentials for heavy-ion fusion cross sections. *Nuclear Physics A,* 979, pp.237-250.

Ghodsi, O.N., and Daei-Ataollah, A., 2016. Systematic study of α decay using various versions of the proximity formalism. *Physical Review C,* 93(2), p.024612.

Guo, C.L., Zhang, G.L., and Le, X.Y., 2013. Study of the universal function of nuclear proximity potential from density-dependent nucleon–nucleon interaction. *Nuclear Physics A*, 897, pp.54-61.

Hagino, K., and Maeno, Y., 2020. A nuclear periodic table. *Foundations of Chemistry,* 22(2), pp.267-273.

Ikezoe, H., Satou, K., Mitsuoka, S.I., Nishio, K., Tsuruta, K., Jeong, S.C., and Lin, C.J., 2004. Effect of closed shell structure on heavy-ion fusion reactions. *Progress of Theoretical Physics Supplement,* 154, pp.45-52.

Kim, T.K., 2017. Understanding one-way ANOVA using conceptual figures. *Korean Journal of Anesthesiology,* 70(1), pp.22.

Lu, Z., and Yuan, K.H., 2010. Welch's t test. In: Salkind, N.J., Eds. *Encyclopedia of Research Design.* Sage, Thousand Oaks, CA, pp.1620-1623.

Manjunatha, H.C., Sowmya, N., Seenappa, L., Damodara Gupta, P.S., and Manjunatha, N., 2023. Heavy ion fusion of spherical nuclei. *Chinese Physics C,* 47(10), pp.104104.

Mathews, J.H., and Fink, K.D., 2004. *Numerical Methods using Matlab*. Pearson Prentice Hall, Upper Saddle River, NJ.

Mişicu, Ş., and Esbensen, H., 2007. Signature of shallow potentials in deep sub-barrier fusion reactions. *Physical Review C-Nuclear Physics,* 75(3), p.034606.

Neideen, T., and Brasel, K., 2007. Understanding statistical tests. *Journal of Surgical Education,* 64(2), pp.93-96.

Nelder, J.A., and Mead, R., 1965. A simplex method for function minimization. *The Computer Journal,* 7(4), pp.308-313.

Ostertagova, E., and Ostertag, O., 2013. Methodology and application of one-way ANOVA. *American Journal of Mechanical Engineering,* 1, pp.256-261.

Othman, B.M., Hussein, A.M., and Taqi, A.H., 2023. Effect of diffuseness parameter on the fusion cross-section of closed-shell nuclei. *Rafidain Journal of Science,* 32(2), pp.53-63.

Recchia, F., Chiara, C.J., Janssens, R.V.F., Weisshaar, D., Gade, A., Walters, W.B., Albers, M., Alcorta, M., Bader, V.M., Baugher, T., Bazin, D., Berryman, J.S., Bertone, P.F., Brown, B.A., Campbell, C.M., Carpenter, M.P., Chen, J., Crawford, H.L., David, H.M., Doherty, D.T., Hoffman, C.R., Kondev, F.G., Korichi, A., Langer, C., Larson, N., Lauritsen, T., Liddick, S.N., Lunderberg, E., Macchiavelli, A.O., Noji, S., Prokop, C., Rogers, A.M., Seweryniak, D., Stroberg, S.R., Suchyta, S., Williams, S., Wimmer, K., and Zhu, S., 2013. Configuration mixing and relative transition rates between low-spin states in 68Ni. *Physical Review C,* 88(4), p.041302.

Sargsyan, V.V., Scamps, G., Adamian, G.G., Antonenko, N.V., and Lacroix, D., 2013. Neutron-pair transfer in the sub-barrier capture process. *Physical Review C,* 88(6), p.064601.

Thiha, K., and Lwin, N.W., 2012. Effects of Different Potential Models for the $^{16}O+^{144,154}Sm$ Fusion Reactions. *Universities Research Journal,* 5(1), pp.257-268.

Tukey, J.W., 1953. *The Problem of Multiple Comparisons*. *Multiple Comparisons*. Princeton University, New Jersey.

Umar, A.S., and Oberacker, V.E., 2007. $^{64}Ni + ^{132}Sn$ fusion within the density-constrained time-dependent Hartree-Fock formalism. *Physical Review C-Nuclear Physics,* 76(1), p.014614.

Yulianto, Y., and Zu'ud, Z., 2018. Numerical study of fusion cross sections for $^{12}C+^{12}C$ and $^{16}O+^{16}O$ reactions by using wong formula. *Jurnal Fisika FLUX,* 15, p.105.

Zanganeh, V., Gharaei, R., and Izadpanah, A.M., 2019. Comparative study for different nuclear proximity potentials applied to quasi-elastic scattering and fusion reactions. *Nuclear Physics A,* 992, p.121637.

Zhang, G.L., Liu, X.X., and Lin, C.J., 2014. Systematic analysis of the effect of a positive *Q*-value neutron transfer in fusion reactions. *Physical Review C,* 89(5), p.054602.

Zhang, G.L., Yao, Y.J., Guo, M.F., Pan, M., Zhang, G.X., and Liu, X.X., 2016. Comparative studies for different proximity potentials applied to large cluster radioactivity of nuclei. *Nuclear Physics A,* 951, pp.86-96.

Zhang, G.L., Zheng, H.B., and Qu, W.W., 2013. Study of the universal function of nuclear proximity potential between α and nuclei from density-dependent nucleon-nucleon interaction. *The European Physical Journal A*, 49(10), p.10.